

# Compressed sensing of mono-static and multi-static SAR

Ivana Stojanovic<sup>a</sup>, W. Clem Karl<sup>b</sup>, Mujdat Cetin<sup>c</sup>,

<sup>a,b</sup>ECE Department, Boston University, Boston, USA

<sup>c</sup>Sabanci University, Istanbul, Turkey

## ABSTRACT

In this paper we study the impact of sparse aperture data collection of a SAR sensor on reconstruction quality of a scene of interest. Different mono and multi-static SAR measurement configurations produce different Fourier sampling patterns. These patterns reflect different spectral and spatial diversity trade-offs that must be made during task planning. Compressed sensing theory argues that the mutual coherence of the measurement probes is related to the reconstruction performance of sparse domains. With this motivation we compare the mutual coherence and corresponding reconstruction behavior of various mono-static and ultra-narrow band multi-static configurations, which trade-off frequency for geometric diversity. We investigate if such simple metrics are related to SAR reconstruction quality in an obvious way.

**Keywords:** SAR, sparse reconstruction, mutual coherence, mono-static, multi-static

## 1. INTRODUCTION

Synthetic aperture radar (SAR) is a remote sensing system capable of producing high-resolution imagery of target scenes independent of time of day, distance, and weather. Conventional SAR radars are mono-static, with collocated transmit and receive antenna elements. These SAR sensors coherently process multiple, sequential observations of a scene under the assumption that the scene is static. Imaging resolution is determined by the bandwidth of the transmitted signals and the size of the synthesized antenna. Greater resolution requires wider bandwidths and larger aspect angles obtained from a longer baseline observation interval. An alternative SAR sensing approach is based on multi-static or MIMO radar configurations, wherein spatially dispersed transmitters and receivers sense the scene. Such configurations provide the opportunity for spatial as well as frequency diversity and offer potential advantages in flexible sensor planning, sensing time reduction, and jamming robustness.

To exploit the promise of multi-static sensing robust methods of reconstructing imagery obtained from more general multi-static configurations are needed, as well as tools to understand and evaluate the performance of various sensor configuration choices in a straight forward, tractable manner. Recently the area known as compressed sensing (CS)<sup>1,2</sup> has received much attention in the signal processing field. Compressed sensing seeks to acquire as few measurements as possible about an unknown signal, and given these measurements, reconstruct the signal either exactly or with provably small probability of error. Interestingly, the reconstruction methods used in CS are related to sparsity-constrained, non-quadratic regularization. The compressed sensing literature has demonstrated accurate signal reconstructions from measurement of extremely few, but randomly chosen Fourier samples of a signal.<sup>2,3</sup> Since both mono and multi-static SAR sensing can be viewed as obtaining samples of the spatial Fourier transform of the scattering field,<sup>4</sup> these results suggest interesting opportunities for SAR sensing. More generally, CS theory relates the accurate reconstruction of a signal to the mutual coherence of the corresponding measurement operator.

In this work we examine the implications of different mono and multi-static measurement configurations on SAR reconstruction performance. In particular, we examine different wide-band mono-static and narrow-band multi-static configurations, which trade off frequency and geometric diversity. We examine how the mutual coherence of the corresponding measurement operator is affected by these different SAR sensing configurations and investigate how such simple metrics are related to reconstruction quality.

The use of sparsity constrained reconstructions for SAR image formation was first presented in,<sup>5</sup> although not within the compressed sensing framework. More recently, there have been several applications of compressed sensing ideas to radar.<sup>6-9</sup> The authors in <sup>6</sup> accurately reconstruct a small number of targets on a time-frequency

plane by transmitting a sufficiently incoherent pulse and employing the techniques of compressed sensing. The authors in<sup>8</sup> propose the use of chirp pulses and pseudo-random sequences for compressed sensing with imaging radars. A compressed sensing technique for a synthetic aperture radar is also discussed in,<sup>7</sup> where the authors obtain measurements by random subsampling of a regular aspect-frequency grid in  $\mathbf{k}$ -space. In our paper, we extend compressed sensing treatments to the multi-static scenario and investigate how mutual coherence of the measurement operator relates to reconstruction quality.

In Section 2 we provide an overview of compressed sensing. Section 3 describes synthetic aperture radar imaging model we use and its application to compressed sensing. We present experimental results in Section 4 relating mutual coherence and the reconstruction quality.

## 2. COMPRESSED SENSING OVERVIEW

Consider a family of signals  $\mathbf{s} \in \mathbf{S} \subset \mathcal{R}^{N \times 1}$ , known to have sparse representation in a dictionary  $\mathbf{D} \in \mathcal{R}^{N \times K}$ . These signals can be represented as  $\mathbf{s} = \mathbf{D}\alpha$ , where  $\alpha \in \mathcal{R}^{K \times 1}$  is a sparse vector, such that the number of its non-zero components satisfies  $\|\alpha\|_0 \leq T \ll K$ . Compressed sensing measures  $M$ ,  $T < M \ll K$ , projections of such a signal, then exploits its sparsity to obtain a reliable reconstruction. To represent this problem mathematically, let  $\mathbf{r} \in \mathcal{R}^{M \times 1}$  represent the measured signal,  $\mathbf{P} \in \mathcal{R}^{M \times N}$  the sensing (projection) matrix such that  $M \ll K$  and  $\mathbf{r} = \mathbf{P}\mathbf{s} = \mathbf{P}\mathbf{D}\alpha = \mathbf{\Phi}\alpha$ . Since  $M \ll K$  this set of equations is extremely under-determined, and many solutions are possible. To overcome this, a sparse solution with only a few non-zero elements is sought.

While optimal design of the dictionary  $\mathbf{\Phi}$  is a topic of interest in compressed sensing, let's first assume that the dictionary is given. For the given  $\mathbf{\Phi}$ , the problem is to find an optimally sparse solution. A direct formulation of this problem can be given as:

$$\min_{\alpha} \|\alpha\|_0 \quad \text{s.t.} \quad \mathbf{r} = \mathbf{\Phi}\alpha,$$

where  $\|\cdot\|_0$  denotes the  $l_0$  norm, which counts the number of non-zero elements of the argument. Unfortunately, this formulation is computationally difficult to solve, as it involves NP-hard enumerative search. The convex relaxation approach relies on the fact that besides the  $l_0$  norm, the  $l_1$  norm also promotes sparsity in a solution. The  $l_1$  norm is defined as  $\|\alpha\|_1 = \left(\sum_{i=1}^K |(\alpha)_i|\right)$ , where  $(\alpha)_i$  is the  $i$ -th element of  $\alpha$ . This norm is a convex function of its arguments. The relaxed version of the problem then takes the form:

$$\min_{\alpha} \|\alpha\|_1 \quad \text{s.t.} \quad \mathbf{r} = \mathbf{\Phi}\alpha,$$

which is essentially a linear program (LP). The use of this formulation has also been motivated by the fact that under certain conditions on the overcomplete dictionary  $\mathbf{\Phi}$ , the original problem and the relaxed version can be shown to have the same solution.<sup>10</sup>

When the signal  $\mathbf{r}$  is noisy, the signal representation problem becomes a signal approximation problem. The convex relaxation formulation of the noisy signal approximation problem is given by:

$$\min_{\alpha} \|\alpha\|_1 \quad \text{s.t.} \quad \|\mathbf{r} - \mathbf{\Phi}\alpha\|_2^2 \leq \delta, \tag{1}$$

where  $\delta$  represents a small noise allowance. Instead of satisfying the relationship exactly, the solution coefficient vector  $\alpha$  is allowed to satisfy the relationship approximately. This problem is known in the literature as noisy basis pursuit.<sup>11</sup> Fast approximate algorithms for the compressed sensing reconstruction given by (1) have also been developed, many of them belonging to a family of matching pursuit algorithms. Note that the problem (1) can also be cast as the following regularization problem for an appropriately chosen parameter  $\lambda$ :

$$\min_{\alpha} \|\mathbf{r} - \mathbf{\Phi}\alpha\|_2^2 + \lambda\|\alpha\|_1. \tag{2}$$

Recent work in compressed sensing established that accurate reconstructions can be obtained with high probability even when only  $\mathcal{O}(T)$  measurements are obtained.<sup>1,2</sup> In particular it was shown that the number of measurements obtained should satisfy

$$M \geq C_{\delta} T \log(K),$$

with an appropriate coefficient  $C_\delta$ , that depends on desired accuracy of the reconstruction. These results require that the sensing matrix  $\Phi$  satisfy the so-called restricted isometry property.<sup>2</sup> The restricted isometry property requires that all sub-matrices containing up to  $T$  columns of the matrix  $\Phi$  are near-isometries. Direct design of  $\Phi$  (and thus  $\mathbf{P}$  and  $\mathbf{D}$ ) based on this property is challenging, as it is combinatorial in nature. Thus, most of the work in CS simply assumes that the projections  $\mathbf{P}$  are drawn at random, as such random projections can be shown to satisfy the required property.

An alternative approach is to focus on the so called mutual coherence of the elements of the sensing matrix  $\Phi$ , seeking configurations with low mutual coherence. This measure is simple to compute, though less directly connected to performance. The mutual coherence  $\mu(\Phi)$  of the sensing matrix  $\Phi$  is formally defined as:<sup>12,13</sup>

$$\mu(\Phi) = \max_{i \neq j} \frac{|\mathbf{a}_i^T \mathbf{a}_j|}{\|\mathbf{a}_i\| \|\mathbf{a}_j\|}, \quad (3)$$

where  $\mathbf{a}_i$  is the  $i$ -th column of the matrix  $\Phi$ . Equivalently, the mutual coherence is the largest non-diagonal entry of the column normalized Gram matrix  $\mathbf{G} = \Phi^T \Phi$ , representing the worst case (that is, largest) similarity between the sensing columns. Orthonormal bases have zero mutual coherence and an overcomplete dictionary with a small mutual coherence is taken to be incoherent. Large mutual coherence indicates a presence of two closely related columns that may confuse reconstruction algorithms.

The mutual coherence gives a guarantee, although pessimistic, that the basis pursuit reconstruction algorithm solution employing  $l_1$  relaxation of the  $l_o$  norm is exactly the optimal solution.<sup>10,13</sup> Namely, the signal  $\mathbf{s}$  is perfectly recovered by both methods provided that the representation  $\alpha$  satisfies the requirement:<sup>10,13</sup>

$$\|\alpha\|_0 < \frac{1}{2} \left( 1 + \frac{1}{\mu(\Phi)} \right).$$

This condition is pessimistic as it guarantees the worst-case reconstruction, i.e. it guarantees zero-error recovery of *any* signal satisfying the above requirement. In general, successful compressed sensing recovery is possible for a significantly larger class of signals by introducing a small probability of error. However, one can aim to optimize the projection probes such that the mutual coherence is minimized in order to implicitly enlarge a class of signals with successful compressed sensing recovery.<sup>14</sup>

Finally, we note that it is known that Fourier measurements represent good projections for compressed sensing of sparse point like signals,<sup>2</sup> when  $\Phi$  represents random undersampling of the spatial frequency data. This suggests a natural application to the SAR sensing problem. In particular, we examine several choices of mono and multi-static SAR sensing and compare their corresponding mutual coherence and reconstruction quality in an effort to better understand their behavior. In the case of SAR, both the sensing matrix and the unknown signal are complex valued, but one can easily translate such case into the standard compressed sensing framework developed for real signals. Alternatively, one can seek solutions that are sparse directly in magnitude, but we do not pursue that route in this paper.

### 3. COMPRESSED SENSING IN SAR

#### 3.1 Signal model

We consider a general multi-static system with spatially distributed transmit and receive antenna elements within a cone positioned at the center of a scene of interest. The mono-static case, with collocated transmit and receive elements, is obtained as a special case of this multi-static model. The scene of interest is modeled by a set of point scatterers reflecting impinging electromagnetic waves isotropically to all receivers within the cone. The reflection coefficient of the point scatterer is a complex number with an unknown amplitude and a random phase.<sup>4</sup> The receiver coherently processes the observations of all receivers across all snapshots, i.e. pulses.

We introduce a coordinate system with the origin in the center of the area of interest and, for simplicity, model the scene as two dimensional. Figure 1 illustrates this set up. The relative size of the scene is assumed to be small compared to distances from the origin of the coordinate system to all transmitter and receivers, such

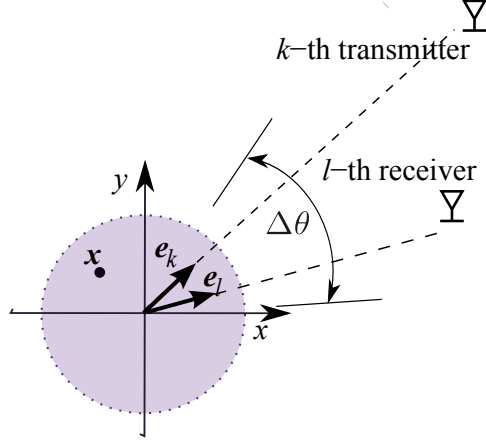


Figure 1. Geometry of the  $kl$ -th transmit-receive pair with respect to the scene of interest. All transmit and receive pairs are restricted to lie within a cone of the angular extent  $\Delta\theta$ .

that transmit and receive angles would change negligibly if the coordinate origin moved to any point in the scene. Furthermore, we neglect signal propagation attenuation.

Next, we present the received signal model for a pair of spatially separated transmit and receive antenna elements. The complex signal received by the  $l$ -th receiver, located at  $\mathbf{x}_l = [x_l, y_l]^T$ , for the narrow-band excitation from the  $k$ -th transmitter, located at  $\mathbf{x}_k = [x_k, y_k]^T$ , reflected from a point scatterer at the spatial location  $\mathbf{x} = [x, y]^T$  is given by:

$$r_{kl}(t) = s(\mathbf{x}) \gamma_k(t - \tau_{kl}(\mathbf{x})),$$

where  $s(\mathbf{x})$  is the reflectivity of the scatterer,  $\gamma_k(t)$  is the transmitted waveform from the  $k$ -th transmitter, and  $\tau_{kl}(\mathbf{x})$  is the propagation delay from the transmitter to the scatterer and back from the scatterer to the receiver, i.e.

$$\tau_{kl} = \frac{1}{c} (\|\mathbf{x}_k - \mathbf{x}\| + \|\mathbf{x}_l - \mathbf{x}\|), \quad (4)$$

where  $c$  is the speed of light and  $\|\cdot\|$  represents the Euclidean norm.

For extended scenes, multiple scatterers are simultaneously illuminated and have their collective response  $q_{kl}(\rho)$  registered at the receive antenna with the same delay.<sup>15</sup> The collection of such scatterers satisfies  $\{\mathbf{x} | c\tau_{kl}(\mathbf{x}) = \rho\}$ . The so-called range profile  $q_{kl}(\rho)$  is an aggregate response at each delay or range and is given by:

$$q_{kl}(\rho) = \int_{\|\mathbf{x}\| \leq L} s(\mathbf{x}) \delta(\rho - c\tau_{kl}(\mathbf{x})) d\mathbf{x}.$$

The overall received signal from the entire ground patch is assumed to be a superposition of the returns from all the scattering centers and is given by:

$$r_{kl}(t) = \int_{-L}^L q_{kl}(\rho) \gamma_k\left(t - \frac{\rho}{c}\right) d\rho = \int_{\|\mathbf{x}\| \leq L} s(\mathbf{x}) \gamma_k(t - \tau_{kl}(\mathbf{x})) d\mathbf{x}, \quad (5)$$

where  $\tau_{kl}(\mathbf{x})$  is given in (4).

For narrow-band waveforms, defined by  $\gamma_k(t) = \tilde{\gamma}_k(t) e^{-j\omega_k t}$ , where  $\tilde{\gamma}_k(t)$  is the low-pass, slowly varying signal and  $\omega_k$  the carrier frequency, we can write:

$$r_{kl}(t) = \int_{\|\mathbf{x}\| \leq L} s(\mathbf{x}) e^{-j\omega_k(t - \tau_{kl}(\mathbf{x}))} \tilde{\gamma}_k(t - \tau_{kl}(\mathbf{x})) d\mathbf{x}.$$

In the far-field case, in which the transmitter-to-scatterer and scatterer-to-receiver distances are large in comparison with the scene dimensions, we can use the first order Taylor series expansion to approximate the propagation delay  $\tau_{kl}(\mathbf{x})$  as:

$$\begin{aligned}\tau_{kl}(\mathbf{x}) &= \frac{1}{c} \left( \|\mathbf{x}_k\| - \mathbf{x}^T \frac{\mathbf{x}_k}{\|\mathbf{x}_k\|} + \|\mathbf{x}_l\| - \mathbf{x}^T \frac{\mathbf{x}_l}{\|\mathbf{x}_l\|} + O(\|\mathbf{x}\|^2/\|\mathbf{x}_k\|) + O(\|\mathbf{x}\|^2/\|\mathbf{x}_l\|) \right) \\ &\approx \frac{1}{c} (\|\mathbf{x}_k\| + \|\mathbf{x}_l\| - \mathbf{x}^T(\mathbf{e}_k + \mathbf{e}_l)) \\ &= \tau_{kl}(\mathbf{0}) - \frac{1}{c} \mathbf{x}^T \mathbf{e}_{kl},\end{aligned}$$

where  $\mathbf{e}_k = [\cos \phi_k, \sin \phi_k]^T$  and  $\mathbf{e}_l = [\cos \phi_l, \sin \phi_l]^T$  are unit vectors in the direction of the  $k$ -th transmitter and  $l$ -th receiver respectively, and  $\tau_{kl}(\mathbf{0})$  is the transmitter-origin-receiver propagation delay, which is known. Thus, the first-order propagation delay approximation is determined by the projection of a scatterer's location onto the  $kl$ -th transmit-receiver pair's bi-static range vector  $\mathbf{e}_{kl} \doteq \mathbf{e}_k + \mathbf{e}_l$ .

Finally, under the far-field scenario, i.e. for  $\|\mathbf{x}\| \ll \|\mathbf{x}_k\|$ ,  $\|\mathbf{x}\| \ll \|\mathbf{x}_l\|$ , and  $\omega_k/c\|\mathbf{x}\|^2 \ll \|\mathbf{x}_k\|$ ,  $\omega_k/c\|\mathbf{x}\|^2 \ll \|\mathbf{x}_l\|$ , we arrive at the following approximation of the received signal:

$$r_{kl}(t) \approx e^{-j\omega_k(t-\tau_{kl}(\mathbf{0}))} \int_{\|\mathbf{x}\| \leq L} s(\mathbf{x}) e^{-j\frac{\omega_k}{c} \mathbf{x}^T \mathbf{e}_{kl}} \tilde{\gamma}_k \left( t - \tau_{kl}(\mathbf{0}) + \frac{1}{c} \mathbf{x}^T \mathbf{e}_{kl} \right) d\mathbf{x}. \quad (6)$$

The received signal model for the mono-static configuration, i.e. the case with collocated transmit-receiver pairs, is obtained by following the same derivation and setting  $\mathbf{x}_k = \mathbf{x}_l$ .

### 3.2 Transmitted waveforms

The chirp signal is the most commonly used spotlight SAR pulse,<sup>4</sup> given by

$$\gamma_k(t) = \begin{cases} e^{j\alpha_k t^2} \cdot e^{j\omega_k t}, & -\frac{\tau_c}{2} \leq t \leq \frac{\tau_c}{2} \\ 0 & \text{otherwise} \end{cases}$$

where  $\omega_k$  is the center frequency and  $\alpha_k$  is the so-called chirp rate of the  $k$ -th transmit element. The frequencies encoded by the chirp signal extend from  $\omega_k - \alpha_k \tau_c$  to  $\omega_k + \alpha_k \tau_c$ , such that the bandwidth of this signal is given by  $B_k = \frac{\alpha_k \tau_c}{\pi}$ . The narrow-band assumption of Section 3.1 is satisfied by choosing the chirp signal parameters such that  $2\pi B_k/\omega_k \ll 1$ . Ultra-narrow band waveforms are special cases of the chirp signal obtained by setting  $\alpha_k = 0$ .

We use this transmitted chirp signal in (6) and apply typical demodulation and baseband processing. In particular, the received signal is mixed with the transmitted signal referenced to the origin of the scene  $e^{-j[\omega_k(t-\tau_{kl}(\mathbf{x}_o)) + \alpha_k(t-\tau_{kl}(\mathbf{x}_o))^2]}$ , and then low-pass filtered. If the quadratic phase error is ignored,<sup>4</sup> we obtain the following observed signal model:

$$r_{kl}(t) \approx \int_{\|\mathbf{x}\| < L} s(\mathbf{x}) e^{-j\Omega_{kl}(t) \mathbf{x}^T \mathbf{e}_{kl}} d\mathbf{x}, \quad (7)$$

where  $\Omega_{kl}(t) = \frac{1}{c} [\omega_k - 2\alpha_k(t - \tau_{kl}(\mathbf{x}_o))]$ , depends on the frequency content of the transmitted waveform.

### 3.3 Discrete model

A discrete version of the model in (7) can be obtained by discretizing the spatial variable  $\mathbf{x}$  and sampling in time which, in the presence of receiver noise  $\mathbf{n}$ , becomes:

$$\mathbf{r} = \sum_{p=1}^N \Phi_p s_p + \mathbf{n} = \Phi \mathbf{s} + \mathbf{n}. \quad (8)$$

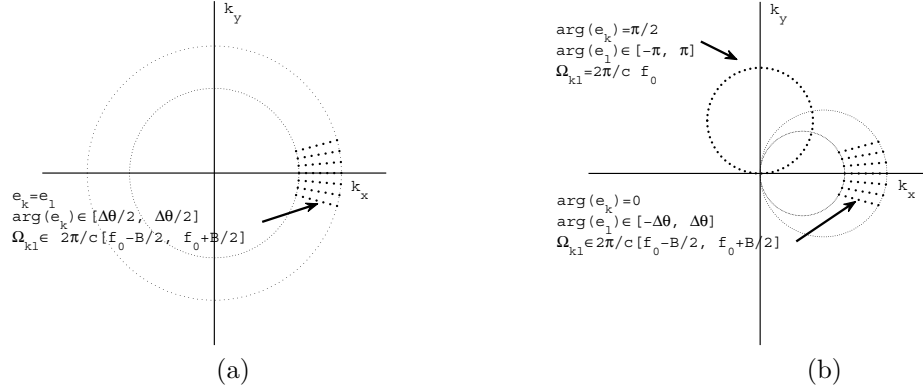


Figure 2. Illustration of the generic  $\mathbf{k}$ -space support for different configurations: (a) mono-static and (b) multi-static.

In this equation,  $\mathbf{r} \in \mathcal{C}^{M \times 1}$  represents the observed, thus known, set of return signals at all receivers across time. Its elements are indexed by the tuple  $(k, l, t_s)$ , with  $t_s$  being the sampling times associated with the  $kl$ -th transmit-receive pair. Thus, the discrete model implicitly assumes that the probes from different transmitters are separable at each receiver. This can be achieved by orthogonal waveform design or by ensuring sequential transmission. The reflectivity of the  $p$ -th spatial cell or pixel is denoted by  $s_p \in \mathcal{C}^{1 \times 1}$  and  $\Phi_p$  is the column vector capturing the contribution to the received signal of a reflector that is located in the  $p$ -th pixel.

### 3.4 Sparse Reconstruction-Based Inversion

The underlying scattering field  $\mathbf{s}$  is complex valued, as is the observed SAR data, while the standard CS framework has been developed for real valued signals. We can map the SAR case into the standard CS framework by breaking the problem into its real and imaginary parts as follows:

$$\tilde{\mathbf{r}} = \begin{bmatrix} \Re \mathbf{r} \\ \Im \mathbf{r} \end{bmatrix}, \quad \tilde{\Phi} = \begin{bmatrix} \Re \Phi & -\Im \Phi \\ \Im \Phi & \Re \Phi \end{bmatrix}, \quad \tilde{\mathbf{s}} = \begin{bmatrix} \Re \mathbf{s} \\ \Im \mathbf{s} \end{bmatrix}. \quad (9)$$

Based on this decomposition, we formulate the image formation process as the following sparsity constrained optimization problem:

$$\hat{\tilde{\mathbf{s}}} = \arg \min_{\tilde{\mathbf{s}}} \|\tilde{\mathbf{r}} - \tilde{\Phi} \tilde{\mathbf{s}}\|_2^2 + \lambda \|\tilde{\mathbf{s}}\|_1^1.$$

This formulation has been shown to produce desirable reconstruction in previous SAR work, and is in keeping with recent inversion methods used in the compressed sensing literature. Note that this problem leads to a standard linear programming problem.

### 3.5 Sampling Configurations

The observation equation (7) represents the 2-D Fourier transform of the spatial reflectivity function, evaluated at the discrete set of the spatial frequency vectors  $\mathbf{k} \doteq [k_x, k_y]^T$  given by

$$\mathbf{k}_{k,l,t_s} = \Omega_{kl}(t_s) \mathbf{e}_{kl} = \Omega_{kl}(t_s) (\mathbf{e}_k + \mathbf{e}_l). \quad (10)$$

Based on this model, a SAR sensing configuration can be associated with its Fourier spatial sampling pattern in both the mono-static<sup>4</sup> and multi-static<sup>16</sup> cases. For example, recall that  $\mathbf{e}_k$  and  $\mathbf{e}_l$  are the unit vectors in the direction of the  $k$ -th transmitter and the  $l$ -th receiver. For the mono-static case these two vectors coincide, i.e.  $\mathbf{e}_k = \mathbf{e}_l$  and when  $t_s$  is fixed, (10) represents the arc of a circle of the radius  $\Omega_{kl}(t_s)$  centered at the origin of the spatial frequency domain, with the extent of the arc determined by the radial span of the vector  $\mathbf{e}_k$ . Changing  $t_s$ , expands or shrinks the circular arc, leading to the familiar key-hole sampling<sup>4</sup> of the conventional mono-static case. Such mono-static  $\mathbf{k}$ -space sampling is illustrated in Figure 2(a).

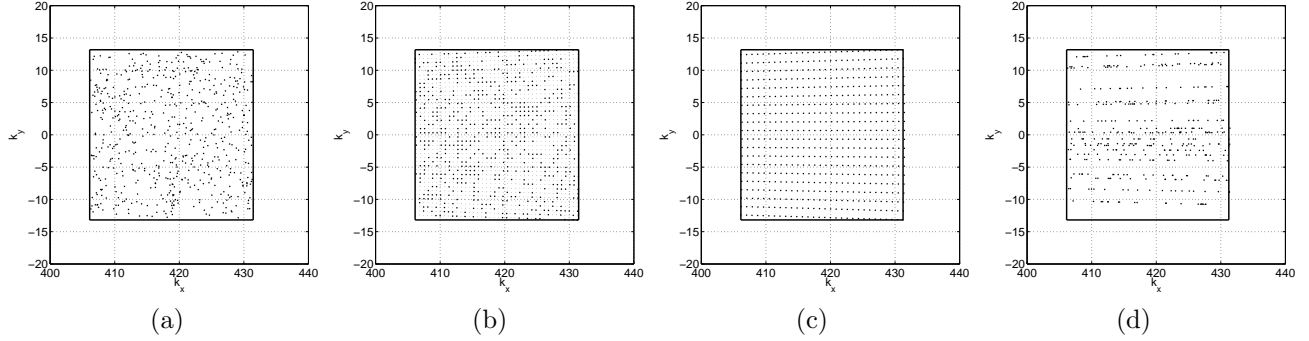


Figure 3. Illustration of the  $\mathbf{k}$ -space sampling patterns for a fixed number of measurements,  $M = 600$ , and a fixed  $\mathbf{k}$ -space extent. (a) (PureRand) Pure random sampling within the given box. (b) (SubsRand) Random subsampling of the conventional, Nyquist grid of  $(N_{tx}, N_f) = (40, 40)$  aspect-frequency points down to 600 points for the mono-static configuration. (c) (RegCS) Mono-static regular aspect-frequency sampling frequency when  $(N_{tx}, N_f) = (20, 30)$ . (d) (RandCS) Mono-static random aspect-frequency sampling when  $(N_{tx}, N_f) = (20, 30)$ . The size of the bounding box is equal in all four cases, and it corresponds to the mono-static configuration with chirp signal transmission ( $f_0 = 10\text{GHz}$ ,  $B = 600\text{MHz}$ ) and aspect angles within the cone  $\arg(\mathbf{e}_k) \in [-\Delta\theta/2, \Delta\theta/2]$ ,  $\Delta\theta = 3.5$  deg.

For the multi-static case, the situation is a bit more complicated. For simplicity, assume that  $\Omega_{kl}(t_s) = \Omega(t_s)$ . At fixed  $t_s$  and fixed  $\mathbf{e}_k$ , (10) also describes an arc of a circle, this time passing through the origin and centered at  $\Omega(t_s)$  along the direction  $\mathbf{e}_k$ . The extent of the arc and its orientation are determined by the radial span of the receiver vector  $\mathbf{e}_l$ . Changing  $t_s$  results in expansion or shrinkage of the circle passing through the origin with its center sliding along the direction  $\mathbf{e}_k$ . Such multi-static  $\mathbf{k}$ -space sampling is illustrated in Figure 2(b).

Thus, different covering patterns of  $\mathbf{k}$ -space are possible with various mono and multi-static sampling configurations. The nominal resolution of a configuration is usually associated with the extent of the  $\mathbf{k}$ -space coverage. In our experiments of Section 4 we will examine different mono and multi-static SAR configurations associated with particular sparse sampling patterns motivated by compressed sensing. In particular, we are interested in seeing how the mutual coherence and reconstruction quality vary for different sparse configurations for a given  $\mathbf{k}$ -space extent (nominal resolution). The cases are described below:

1. (PureRand) Pure random sampling of  $k_x$  and  $k_y$  within a  $\mathbf{k}$ -space box of specified dimensions. This case provides the most randomness in sampling and thus should provide a lower bound on mutual coherence. Note that such sampling may require a large number of sampling probes operationally, so is essentially impractical in practice. This sampling pattern is illustrated in Figure 3(a).
2. (SubsRand) Random subsampling of the conventional, Nyquist grid for the mono-static configuration only.<sup>2,7</sup> The number of aspect-frequency points on the conventional, mono-static grid is determined from Nyquist arguments. For the narrow-angle mono-static configuration, the  $\mathbf{k}$ -sampling grid is close to be rectangular. Given the size of a scene and a desired resolution, radar signal parameters such as signal bandwidth, aspect range, frequency step and aspect step are automatically determined.<sup>4</sup> The signal bandwidth is determined by a desired range resolution and the aspect range is determined by a desired cross-range resolution. Furthermore, the frequency step is inversely proportional to the range dimension of the scene, and similarly, the aspect step is inversely proportional to the cross-range dimension of the scene, resulting in a nominal number of measurements on a regular  $\mathbf{k}$ -space grid. Compressed sampling of such a grid is obtained by random subsampling of points in both dimensions, as illustrated in Figure 3(b). The number of transmitted probes before and after subsampling remains the same with high probability.
3. Compressed sampling in transmit/receive aspect and frequency dimensions. Here, we aim to investigate if reducing the number of transmit probes can mimic the incoherence properties of pure random sampling as closely as possible and yet allow for rapid data collection. Given a desired number of transmitted probes and a total number measurements (less than required for a conventional reconstruction), we consider two cases:

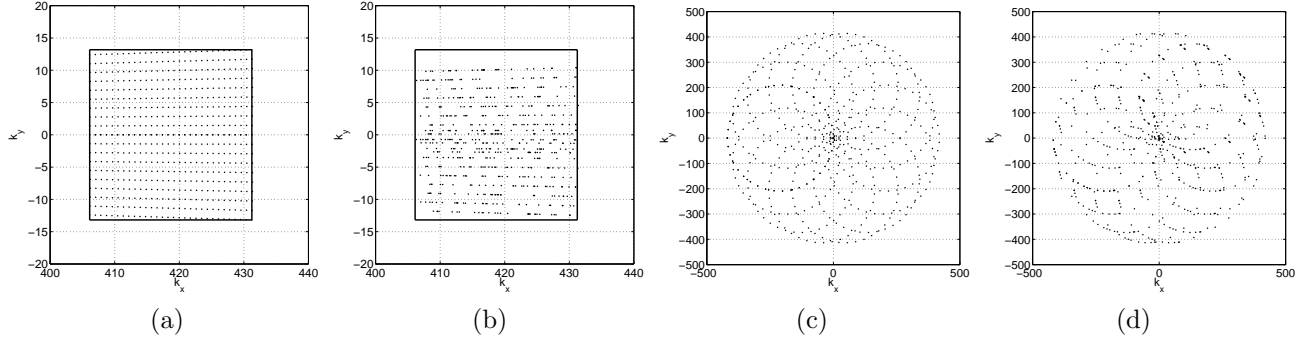


Figure 4. Multi-static  $\mathbf{k}$ -space sampling patterns for a fixed number of measurements,  $M = 600$ . (a) (RegCS) Regular aspect-frequency sampling when  $(N_{tx}, N_{rx}, N_f) = (2, 10, 30)$  for  $\arg(\mathbf{e}_k), \arg(\mathbf{e}_l) \in [-\Delta\theta, \Delta\theta]$ ,  $\Delta\theta = 3.5$  deg and chirp signal transmission with  $f_0 = 10\text{GHz}$ ,  $B = 600\text{MHz}$ . (b) (RandCS) Random aspect-frequency sampling when  $(N_{tx}, N_{rx}, N_f) = (10, 2, 30)$  for the same  $\arg(\mathbf{e}_k), \arg(\mathbf{e}_l)$  range and chirp signal parameters. (c) (RegCS) Regular aspect sampling of circular, ultra-narrow band multi-static SAR when  $(N_{tx}, N_{rx}, N_f) = (15, 40, 1)$  for  $\arg(\mathbf{e}_k), \arg(\mathbf{e}_l) \in [-\pi, \pi]$  and ultra-narrow band probes at  $f_0 = 10\text{GHz}$ . (d) (RandCS) Random aspect sampling of circular, ultra-narrow band multi-static SAR when  $(N_{tx}, N_{rx}, N_f) = (15, 40, 1)$  for the same  $\arg(\mathbf{e}_k), \arg(\mathbf{e}_l)$  range and transmit signal frequency.

- (a) (RegCS) Regular positioning of transmit and receive elements within a specified cone and regular sampling of the returned signal. Illustration is shown in Figure 3(c) for the mono-static and in Figure 4(a),(c) for the multi-static configurations.
- (b) (RandCS) Random uniform positioning of transmit and receive elements within a specified cone and random sampling of the returned signal. This case is illustrated in Figure 3(d) for the mono-static and in Figure 4(b),(d) for the multi-static configurations.

We consider multiple snapshot, non-overlapping transmissions of chirp signals in the mono-static case and ultra-narrow band signals in the multi-static case. In the following, we show simulation results and discuss tradeoff of different configurations in the compressed sensing framework.

## 4. EXPERIMENTAL RESULTS

In this section we present results of our experiments. For each SAR sensing configuration described in Section 3.5 we calculate and display the mutual coherence and an associated average reconstruction error for scenes of various complexity, with complexity captured by a varying number of non-zero scatters in the scene. We consider two cases, the traditional mono-static SAR and the multi-static SAR.

### 4.1 Mono-Static SAR

In this subsection we consider mono-static spotlight SAR imaging of a small ground patch of size  $(D_x, D_y) = (10, 10)\text{m}$ , when observed over a narrow-angle aspect cone of  $\Delta\theta = 3.5$  deg. The transmitted waveforms are chirp signals with  $f_0 = 10\text{GHz}$  and  $B = 600\text{MHz}$ . A nominal Rayleigh range resolution is  $\rho_x = \frac{c}{2B} = .25\text{m}$  and a nominal cross-range resolution is  $\rho_y = \frac{\lambda}{4 \sin(\Delta\theta/2)} = .25\text{m}$ . Assuming that a pixel spacing matches the Rayleigh resolution, we seek to reconstruct a 2D image of the scene with  $40 \times 40$  pixels in each dimension.

In Figure 5(a), we present the mutual coherence as a function of the  $\mathbf{k}$ -space sampling patterns when the number of measurements is fixed to  $M = 600$ . Sampling patterns associated with this sub-section are illustrated in Figure 3. In RegCS and RandCS cases, the number of aspect angles (transmitted probes)  $N_{tx}$  and the number of chirp frequency samples  $N_f$  is varied such that  $M = N_{tx}N_f = 600$ . As indicated earlier, RandCS case assumes that both aspect angles and sampling frequencies are chosen independently and uniformly at random within the allowable range, whereas in RegCS case the aspect step and the frequency step are fixed. In the random subsampling case, SubsRand, the conventional grid of  $(N_{tx}, N_f) = (40, 40)$  points is down-sampled uniformly at random to 600 points. The results of Figure 5(a) indicate that the mutual coherence is minimized

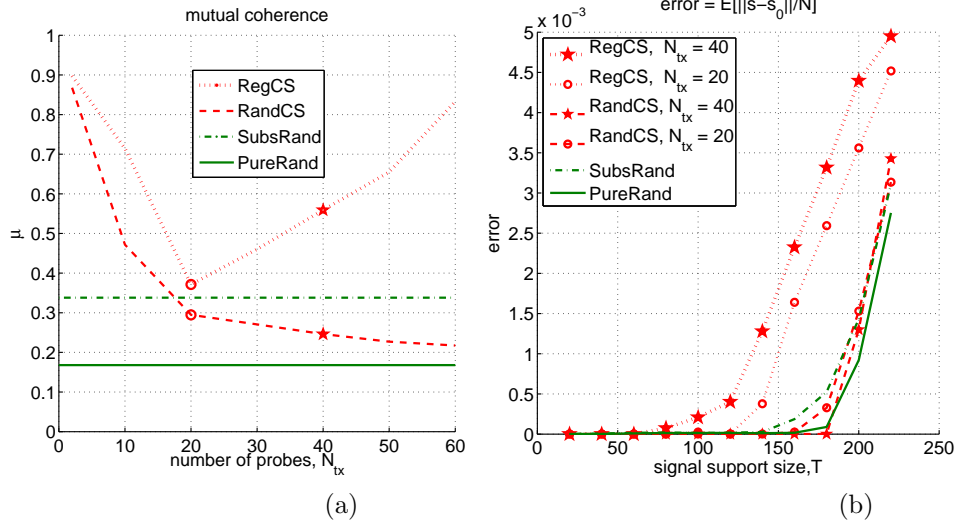


Figure 5. Mutual coherence and reconstruction error for the mono-static SAR when  $M = 600$ . (a) Mutual coherence of different sampling configurations. (b) Average per-pixel reconstruction error for a scene of  $N = 1600$  pixels.

when  $\mathbf{k}$ -space sampling points cover the available  $\mathbf{k}$ -space uniformly at random. The most uniform coverage in RegCS case with  $M = N_{tx}N_f$  measurements is achieved when the ratio of the number of aspect angles to the number of frequency samples is approximately  $N_{tx}/N_f = \Delta K_x/\Delta K_y$ , where  $\Delta K_x$  ( $\Delta K_y$ ) is the  $\mathbf{k}$ -space extent in cross range (range) direction. Furthermore, the slope of  $\mu$  vs.  $N_{tx}$  curve past this point becomes small in RandCS case, indicating that increasing the number of transmitted probes beyond this point should have only a small impact on the reconstruction performance.

In Figure 5(b), we show reconstruction quality as a function of a number of randomly dispersed, non-zero, scatterers in the scene when  $M = 600$ . The reconstruction quality is defined as Monte-Carlo average of an average per-pixel error, i.e.  $\mathcal{E} = E[\|s - s_0\|/N]$ , where  $E$  denotes the expectation and  $N$  the total number of pixels in the scene. In our examples,  $N = 1600$ . The results indicate that as the mutual coherence is lowered, the signal sparsity level at which perfect reconstruction is possible improves significantly. RandCS reconstruction outperforms both SubsRand and RegCS case. Furthermore, RandCS reconstruction quality close to PureRand case is achieved with  $N_{tx} = 20$  probes instead of the nominal  $N_{tx} = 40$ .

In Figure 6, we evaluate the mutual coherence and the reconstruction quality as a function of the number of measurements,  $M$ , when signal sparsity is fixed such that  $T = 160$ . We present plots for the regular, RegCS, and the random, RandCS, cases when  $N_{tx} = 20$  and  $N_{tx} = 40$ . Increasing the number of measurements has a beneficial impact on the mutual coherence and it also reduces the reconstruction error up to a point when accurate reconstruction is achieved. Therefore, accurate reconstruction can be achieved even with the regular sampling, RegCS, and the small number of probes, i.e.  $N_{tx} = 20$ , at the expense of increased frequency sampling. Contrast this to the conventional sampling, SubsRand case, that approximately requires  $N_{tx} = 40$ . Furthermore, the number of measurements needed for the accurate reconstruction is on the order or 4 – 5 times the number of point reflectors in the scene. Although both RegCS and RandCS, sampling can recover the scene perfectly, the random sampling achieves the goal with the smaller number of measurements.

Finally, in Figure 7, we contrast the compressed sensing reconstruction to the conventional filtered back-projection reconstruction with partial and complete data. Filtered back-projection performs very poorly when few observations are available, but it can recover the scene with high quality by significantly increasing the number of measurements.

## 4.2 Multi-Static SAR

In the previous section we studied the impact of different sampling configurations on reconstruction quality in the mono-static case. The major advantage of compressed sensing in the mono-static scenario is the reduced

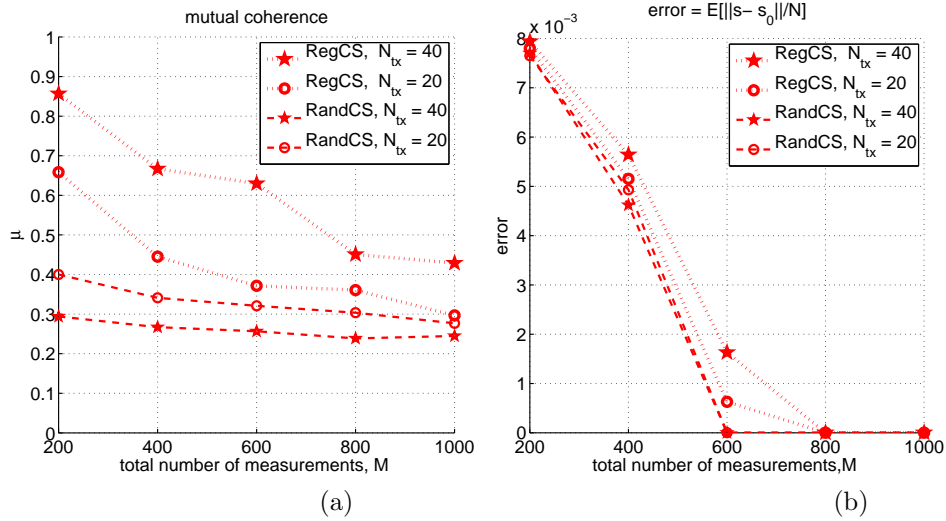


Figure 6. Mutual coherence and reconstruction quality as function of number measurements for RegCS and RandCS mono-static SAR cases where  $M = N_{tx}N_f$ . (a) Mutual coherence. (b) Average per-pixel reconstruction error of  $N = 1600$  pixel scene with  $T = 160$  point reflectors randomly dispersed in the scene.

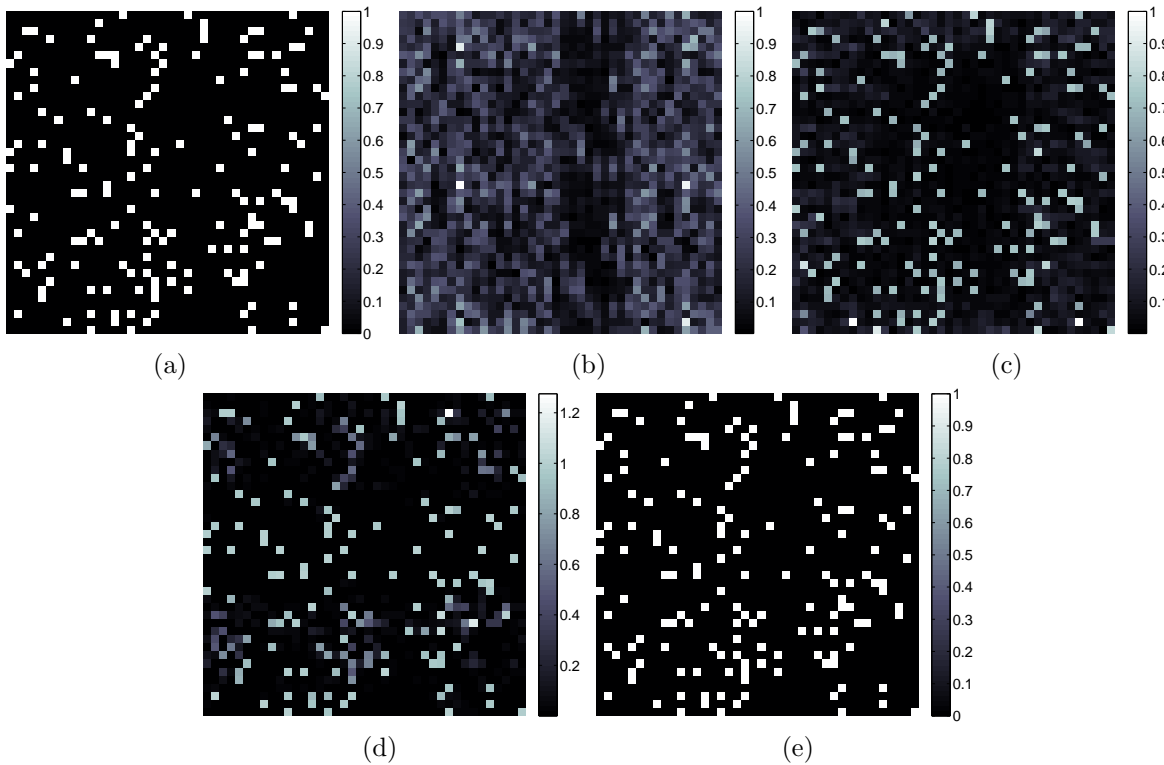


Figure 7. Mono-static SAR sample reconstructions of a scene with  $T = 160$  point reflectors, with complete and partial data. (a) Ground truth, (b) Conventional FBP reconstruction with  $M = 600$ . (c) Conventional FBP with  $M = 12000$ . (d) Sparse reconstruction for RegCS case when  $M = 600$ ,  $N_{tx} = 20$ . (e) Sparse reconstruction for RandCS case when  $M = 600$ ,  $N_{tx} = 20$ .

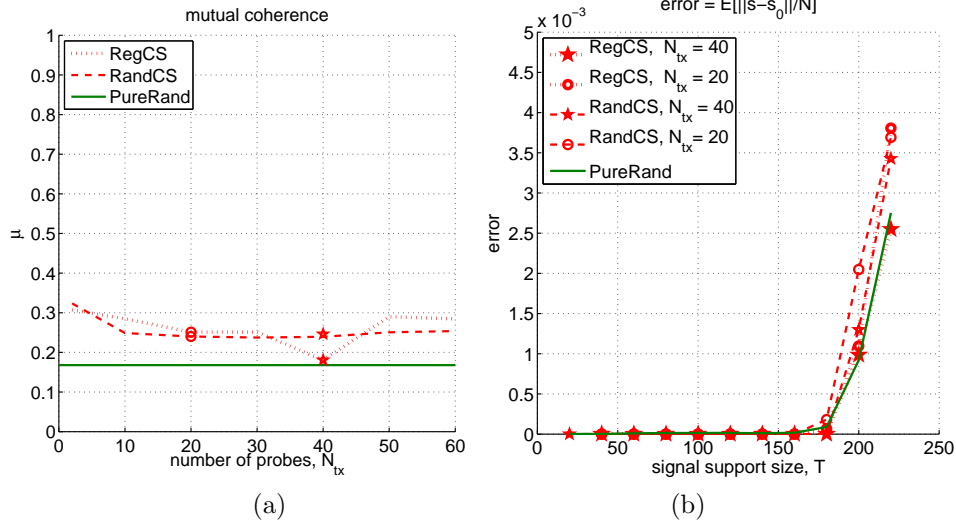


Figure 8. Mutual coherence and reconstruction error for the circular, multi-static SAR when  $M = N_{tx}N_{rx}N_f = 600$  and  $N_f = 1$ . (a) Mutual coherence of different sampling configurations. (b) Average per-pixel reconstruction error.

data storage and the number of transmitted probes. Data collection time can not be reduced, as the mono-static SAR platform covers the whole aspect range sequentially in time. On the other hand, the multi-static SAR has a potential to further reduce the data acquisition time at the expense of having multitude of spatially dispersed transmitters and receivers. Theoretically, there exist many multi-static geometries with similar  $\mathbf{k}$ -space coverage as in the mono-static case, and thus, the equivalent reconstruction result. In Figure 4(a) and Figure 4(b) we demonstrate multi-static  $\mathbf{k}$ -space patterns similar to the ones obtained with the mono-static configurations. Equivalent reconstruction errors are obtained as well, but we omit those plots from the paper.

In an extreme case, we consider a multi-static configuration with transmitters and receivers placed around the scene in the full circle.<sup>16</sup> In Figure 4(c) and Figure 4(d) we show RegCS and RandCS  $\mathbf{k}$ -space sampling configurations, respectively, when transmitted waveforms are ultra-narrow band signals at frequency  $f_o = 10$  GHz. The size of the  $\mathbf{k}$ -space extent is determined solely by the carrier wavelength - reducing the carrier wavelength, results in proportionally smaller coverage<sup>16</sup> and vice versa.

Next, we evaluate the mutual coherence and corresponding reconstruction quality of the circular multi-static SAR for the regular, RegCS, and the random, RandCS, sampling cases. It is well known that due to the holographic properties of spotlight synthetic aperture measurements, the reflectivity magnitude of a given scene can be recovered at the same resolution from many  $\mathbf{k}$ -space regions, as long as the extent of such regions is approximately the same.<sup>4,17</sup> In order to make comparisons to the mono-static case presented earlier, the carrier wavelength is reduced, such that Rayleigh resolutions of the two configurations are approximately the same. Furthermore, as the isotropic scattering is the key for coherent processing and effective imaging, we assume that the isotropic scattering assumption is valid for the circular multi-static configuration as well.

In Figure 8(a), we show the mutual coherence as a function of the number of transmitted probes when  $M = 600 = N_{tx}N_{rx}N_f$ . Both RegCS and RandCS sampling deviates significantly from a regular  $\mathbf{k}$  grid. This translates into a significantly reduced coherence with a very small number of probes when compared to the mono-static case and reconstruction quality close to PureRand sampling case, as illustrated in Figure 8(b). While the random sampling was the key to the improved performance in the mono-static case, the circular multi-static configuration is robust to transmit/receive sensor aspects. Furthermore, when ultra-narrow band pulses are non-overlapping in frequency, all transmitters can transmit simultaneously and the data can be acquired within a duration of a single probe.

## 5. CONCLUSIONS

In this paper we studied different mono-static and multi-static SAR measurement configurations in the context of compressed sensing. The compressed sensing techniques when applied to SAR allow for a reliable sparsity-driven imaging with the dramatically reduced number of transmitted probes and with the total number of data samples required to scale only linearly with the sparsity of the scene. The performance of the sparse reconstruction is primarily determined by a sampling pattern in the spatial-frequency domain. Both mono-static and multi-static configurations can achieve the similar reconstruction performance, as long as their respective mutual coherence is minimized. In the multi-static case, it is straightforward to get to the low coherence either by regular or random aspect-frequency sampling, whereas in the mono-static case random aspect-frequency sampling is preferred. The aspect-frequency randomization enables the mono-static SAR to achieve better reconstruction, with the smaller number of probes than the simple random subsampling of the conventional, Nyquist grid. For partially incoherent scenarios, sparsity-driven imaging quality degrades, but is not completely lost, and it can be recovered by acquiring slightly more data samples. We showed that the similar reconstructions are obtained by 'wide-band' mono-static and ultra-narrow band multi-static configurations, effectively trading off frequency for geometric diversity.

## REFERENCES

- [1] Donoho, D. L., "Compressed sensing," *IEEE Trans. Inform. Theory* **52**(4), 1289–1306 (2006).
- [2] Candes, E. J., Romberg, J., and Tao, T., "Robust uncertainty principles: Exact signal reconstruction from highly incomplete frequency information," *IEEE Trans. Inform. Theory* **52**(2), 489–509 (2006).
- [3] Lustig, M., Donoho, D., and Pauly, J. M., "Sparse MRI: The application of compressed sensing for rapid MR imaging," *Magnetic Resonance in Medicine* **9999** (2007).
- [4] Jakowatz, C. V., Wahl, D. E., Eichel, P. S., Ghiglian, D. C., and Thompson, P. A., [*Spotlight-mode Synthetic Aperture Radar: a Signal Processing Approach*], Kluwer Academic Publishers, Norwell, MA (1996).
- [5] Cetin, M., [*Feature-Enhanced Synthetic Aperture Radar Imaging*], Ph.D. Thesis, Boston University (2001).
- [6] Herman, M. A. and Strohmer, T., "High-resolution radar via compressed sensing," *IEEE Trans. Signal Processing (to appear)* (2009).
- [7] Yoon, Y.-S. and Amin, M. G., "Compressed sensing technique for high-resolution radar imaging," *Signal Processing, Sensor Fusion, and Target Recognition XVII, SPIE* **6968**(1) (2008).
- [8] Baraniuk, R. and Steeghs, P., "Compressive radar imaging," *IEEE Radar Conference* ., 128–133 (2007).
- [9] Bhattacharya, S., Blumensath, T., Mulgrew, B., and Davies, M., "Fast encoding of synthetic aperture radar raw data using compressed sensing," *Statistical Signal Processing, IEEE/SP 14th Workshop on* , 448–452 (2007).
- [10] Donoho, D. L. and Elad, M., "Optimally sparse representation in general (nonorthogonal) dictionaries via  $l_1$  minimization," *Proceedings of the National Academy of Science* **100**(5), 2197–2202 (2003).
- [11] Chen, S. S., Donoho, D. L., and Saunders, M. A., "Atomic decomposition by basis pursuit," *SIAM Journal on Scientific Computing* **20**, 33–61 (1998).
- [12] Candes, E. and Romberg, J., "Sparsity and incoherence in compressive sampling," *Inverse Problems* **23**(3), 969–985 (2007).
- [13] Donoho, D. and Huo, X., "Uncertainty principles and ideal atomic decomposition," *IEEE Trans. Inform. Theory* **47**(7), 2845–2862 (2001).
- [14] Elad, M., "Optimized projections for compressed sensing," *IEEE Trans. Signal Processing* **55**(12), 5695–5702 (2007).
- [15] Rihaczek, A., [*Principles High-Resolution Radar*], IEEE Press, New York (1988).
- [16] Himed, B., Bascom, H., Clancy, J., and Wicks, M. C., "Tomography of moving targets (TMT)," in [*Sensors, Systems, and Next-Generation Satellites*], Fujisada, H., Lurie, J. B., and Weber, K., eds., *Sensors, Systems, and Next-Generation Satellites V* **4540**(1), 608–619, Proc. SPIE (2001).
- [17] Munson, D.C., J. and Sanz, J., "Image reconstruction from frequency-offset Fourier data," *Proceedings of the IEEE* **72**(6), 661–669 (1984).